Frozen-phonon method for state anticrossing situations and its application to zero-point motion effects in diamondoids

Pablo García-Risueño,[1,2,*] Peng Han,[1,3] Surender Kumar,[1] and Gabriel Bester[1,2,†]

[1]*Institute for Physical Chemistry, Universität Hamburg, Luruper Chaussee 149, D-22761 Hamburg, Germany*

[2]*The Hamburg Centre for Ultrafast Imaging, Luruper Chaussee 149, D-22761 Hamburg, Germany*

[3]*Department of Physics, Capital Normal University, Beijing Key Lab for Metamaterials and Devices, Beijing 100048, China*

(Received 15 March 2022; accepted 9 June 2023; published 5 September 2023)

The frozen-phonon method, used to calculate electron-phonon coupling effects, requires calculations of the investigated structure using atomic coordinates displaced according to certain phonon eigenmodes. The process of "freezing in" the specific phonon can bring electronic eigenstates that are energetically close in energy into an anticrossing. This electronic anticrossing effect is, however, unrelated to electron-phonon coupling and needs to be removed if the eigenvalues are used to obtain electron-phonon coupling. We present a procedure for how to deal with these problematic anticrossing situations and apply it to the band gap zero-point motion renormalization of 16 diamondoids and urotropine using different exchange correlation functionals. From the 17 structures, 5 require the correction presented here, leading to a modification of the zero-point renormalization between 4% and 185%. We find gap renormalizations in the range of −150 to −370 meV for diamondoids but only around −40 meV for urotropine.

DOI: 10.1103/PhysRevB.108.125403

I. INTRODUCTION

Understanding the effect that the nuclear motion has on electronic properties has been a challenging scientific problem [1–5] and remains a central topic of solid-state physics and quantum chemistry [6–11]. Electron-phonon (*e*-ph) coupling can be studied with a computational technique referred to as "frozen phonon" (FP). As originally proposed by Dacorogna *et al.* [12] to calculate the *e*-ph coupling matrix elements of bulk aluminum from first principles, the atoms are frozen into the displaced positions they acquire during a certain vibration. The electronic response to the distortion represents the *e*-ph coupling. The method requires, however, large supercells, especially for long-wavelength phonons, which has limited its application. Furthermore, with the rapid development of density functional perturbation theory [13], the frozen-phonon approach has less frequently been used to calculate *e*-ph coupling matrix elements [12,14]. Capaz *et al.* [15] extended the *ab initio* frozen-phonon approach to study the renormalization of the band gap due to zero-point motion (ZPM or ZPR), i.e., the modification of the electronic eigenvalues by a nuclear quantum effect, and the temperature-dependent band gap renormalization. Compared to the "standard" (i.e. its original version) Allen-Heine-Cardona (AHC, sometimes called HAC) theory [16] of ZPR [17] (recently applied to two-dimensional systems [18,19]), the frozen-phonon approach includes the so-called non-rigid-ion Debye-Waller (NRIA DW [20]; also called nondiagonal Debye-Waller [21]) terms missing in the AHC model as well as anharmonic effects of lattice vibration and gives a more accurate description of ZPR [6,21,22]. In recent years, the *ab initio*-based frozen-phonon approach has been used to calculate the ZPR effect and temperature-dependent band gap renormalization in semiconductor nanoclusters [23]; in bulk diamond, Si, and SiC structures [24]; in hexagonal and cubic ice [25]; and in molecular crystals [26]. Moreover, recent developments of the frozen-phonon method include nondiagonal supercells [27,28] and one-shot calculation of temperature-dependent optical spectra [29]. However, the frozen-phonon method suffers, as we intend to demonstrate, from a problem that occurs when the applied deformation (frozen phonon) leads to an anticrossing of the electronic states.

In this paper, we propose a modification of the standard frozen-phonon method [15] in order to properly treat the situation of state anticrossings, which can happen when eigenstates are energetically close to the eigenstate considered and have the same point group symmetry, allowing direct electronic coupling of both states. In this case, the effect of the frozen phonon perturbation can lead to an anticrossing of both electronic states [the energy of the upper (lower) state is raised (lowered) by the perturbation]. This anticrossing is mainly the result of a direct electronic coupling due to the perturbation and only marginally due to the more subtle electron-phonon interaction we seek. Both effects must therefore be disentangled, which is the topic of this work. We illustrate this problem of state mixing and show that four qualitatively different situations can occur. We present a method to circumvent the problems and apply it to 16 carbon-caged nanostructures called *diamondoids* and urotropine, in which the renormalization of the band gap due to electron-vibrational interaction is strong, in the range of a few hundred meV. The electronic anticrossing situation occurs in 5 out of the 17 structures

*risueno@unizar.es

†gabriel.bester@uni-hamburg.de

and requires the correction presented here. The correction modifies the calculated ZPR by 244, 207, 495, 88, and 11 meV for a ZPR of 368, 296, 327, 284, and 331 meV for $C_{14}H_{20}$, $C_{18}H_{24}$, $C_{22}H_{28}$ with C_2 symmetry, $C_{22}H_{28}$ with C_{2h} symmetry, and $C_{38}H_{42}$, respectively.

Moreover, we find that the results using hybrid functionals [Becke three-parameter Lee-Yang-Parr (B3LYP)] are rather different (∼25%) from those of the local-density approximation (LDA) and generalized gradient approximation (GGA) for the renormalizations of the highest occupied molecular orbital (HOMO) and the lowest unoccupied molecular orbital (LUMO) individually but similar to those for the renormalizations of the HOMO-LUMO gap. The results for the HOMO renormalization of urotropine are very different than those for the diamondoids (significantly smaller), a fact that we explain by the lone-pair nature of the HOMO in urotropine.

II. THEORY

A. Standard frozen-phonon approach for ZPR

The phonon theory is based on the solution of the dynamical equation [20]:

$$\sum_{I\alpha} D_{I\alpha,J\alpha'}\, X^{\nu}_{I\alpha} \;=\; \omega_{\nu}^2\, X^{\nu}_{J\alpha'}, \tag{1}$$

where $I, J = 1, \ldots, N_{\rm at}$ (with $N_{\rm at}$ being the number of atoms) are atomic indices, α and α' are their corresponding Cartesian coordinate indices, ν is the phononic index, and X^{ν} are the normal modes of vibration. The dynamical matrix D is defined as

$$D_{I\alpha,J\alpha'} \;=\; \frac{1}{\sqrt{M_I M_J}}\, \frac{\partial^2 \mathcal{E}^{\rm BO}}{\partial R_{I\alpha}\partial R_{J\alpha'}}, \tag{2}$$

where M_I are the atomic masses, $R_{I\alpha}$ are the nuclear coordinates, and $\mathcal{E}^{\rm BO}$ is the Born-Oppenheimer energy surface [20]; ω_{ν}^2 and X^{ν} are the eigenvalues and eigenvectors of the dynamical matrix (ω_{ν} are the phonon frequencies).

The frozen-phonon method [15] is used to calculate the temperature-dependent renormalization of electronic eigenvalues E_n due to vibronic coupling, i.e., the change in the electronic energies due to the vibrational motion of the nuclei. This renormalization is found from finite-difference calculations and is given by

$$\Delta E_n(T) \;=\; \sum_{\nu} \Delta E_n^{\nu}(0)\left(n_{\nu}^{\rm B} + \frac{1}{2}\right), \tag{3}$$

where $n^{\rm B} = (\exp[\omega_{\nu}/T] - 1)^{-1}$ is the Bose-Einstein distribution in atomic units. The $\Delta E_n^{\nu}(0)$ coefficients are

$$\Delta E_n^{\nu}(0) \;=\; \frac{1}{2\omega_{\nu}}\, \frac{d^2}{dh^2}\, E_n[\,\mathbf{x}_0 + h\mathbf{U}^{\nu}\,]|_{h=0}, \tag{4}$$

where h is a displacement parameter (with units of $1/\sqrt{\omega_{\nu}}$), $U^{\nu}_{I\alpha} = X^{\nu}_{I\alpha}/\sqrt{M_I}$ are the phonon eigenmodes, M_I is the mass of the Ith atom, $E_n[\mathbf{x}]$ is the nth electronic eigenvalue at $T = 0$ when the nuclei are at positions given by $\mathbf{x}$ (which is a vector of $3N_{\rm at}$ components), and $\mathbf{x}_0$ is the set of relaxed nuclear positions. Equations (3) and (4) result from performing an average of the electronic eigenvalues assuming parabolic dependence on the nuclear positions (harmonic approximation). A derivation of these equations can be found in Ref. [20]. In the frozen-phonon method, the second derivatives of (4) are solved by finite difference. In this paper we propose to evaluate it using the standard finite-difference equation:

$$\Delta E_n^{\nu}(0) = \frac{E_n[\mathbf{x}_0 + h\mathbf{U}^{\nu}] - 2E_n[\mathbf{x}_0] + E_n[\mathbf{x}_0 - h\mathbf{U}^{\nu}]}{2\,\omega_{\nu}\,h^2}, \tag{5}$$

with h being as small as possible [30], e.g., between 2 and 10 a.u. Note that in Eq. (5) the displacement size is equal for all the vibrational modes (it does not depend on ν because the normal modes are normalized [30]). Our choice [Eq. (5)] is in contrast to the generally used expression [10,15,23,31–35] to calculate the derivatives, in which the displaced positions used in the finite difference are $\mathbf{x}^{\nu}_{\pm} = \mathbf{x}_0 \pm \mathbf{U}^{\nu}/\sqrt{\omega_{\nu}}$ and thus

$$\Delta E_n^{\nu}(0) = \frac{E_n[\mathbf{x}^{\nu}_{+}] - 2E_n[\mathbf{x}_0] \,+\, E_n[\mathbf{x}^{\nu}_{-}]}{2}. \tag{6}$$

Despite its popularity, Eq. (6) performs displacements which are often too large, leading to distortion of the results because of the appearance of crossings of the eigenvalues. In order to remove these possible errors we propose a modified frozen-phonon approach for the calculation of ZPR in nanostructures.

B. Modified frozen-phonon approach for ZPR

In Fig. 1 we show the highest occupied eigenvalues of lower diamondoids ($C_{14}H_{20}$ and $C_{18}H_{24}$) as a function of the displacement parameter h for different vibrational modes. Different problematic situations which arise in the frozen-phonon method include a simple level crossing [Fig. 1(a)], a symmetric anticrossing (avoided crossing) of two levels [Fig. 1(b)], a combined situation of crossing and anticrossing [Fig. 1(c)], and a double anticrossing [where three states couple to each other, as shown in Fig. 1(d)]. The anticrossing situations [Figs. 1(b)–1(d)] are problematic because the curvatures of the h-dependent eigenvalues have a dominant component coming from the anticrossing effect itself instead of the electron-phonon coupling. Indeed, the anticrossing has a dominant contribution from the coupling of both electronic states due to their compatible point group symmetries, which allows them to interact and mix. These anticrossings are not induced by electron-phonon coupling. This becomes obvious from the fact that the anticrossing is happening at zero displacement ($h = 0$), where no phonon is frozen in. As can be seen from Figs. 1(b)–1(d), this electronic coupling effect [e.g., the opening of a gap in Fig. 1(b) at $h = 0$] can be very large and coexists with the electron-phonon coupling effect. Further, note that the linear terms [slopes in, e.g., Fig. 1(a)] are not the quantities required for the calculation of ZPR, but the quadratic dependence [according to Eq. (5)], which is small and actually not noticeable by eye in Fig. 1(b). The linear term cancels in the thermal average. The principal aim of this work is to derive a procedure to disentangle both effects. In Fig. 1(a), a more trivial problem occurs where the states simply cross. In this case one must take care, in the calculation

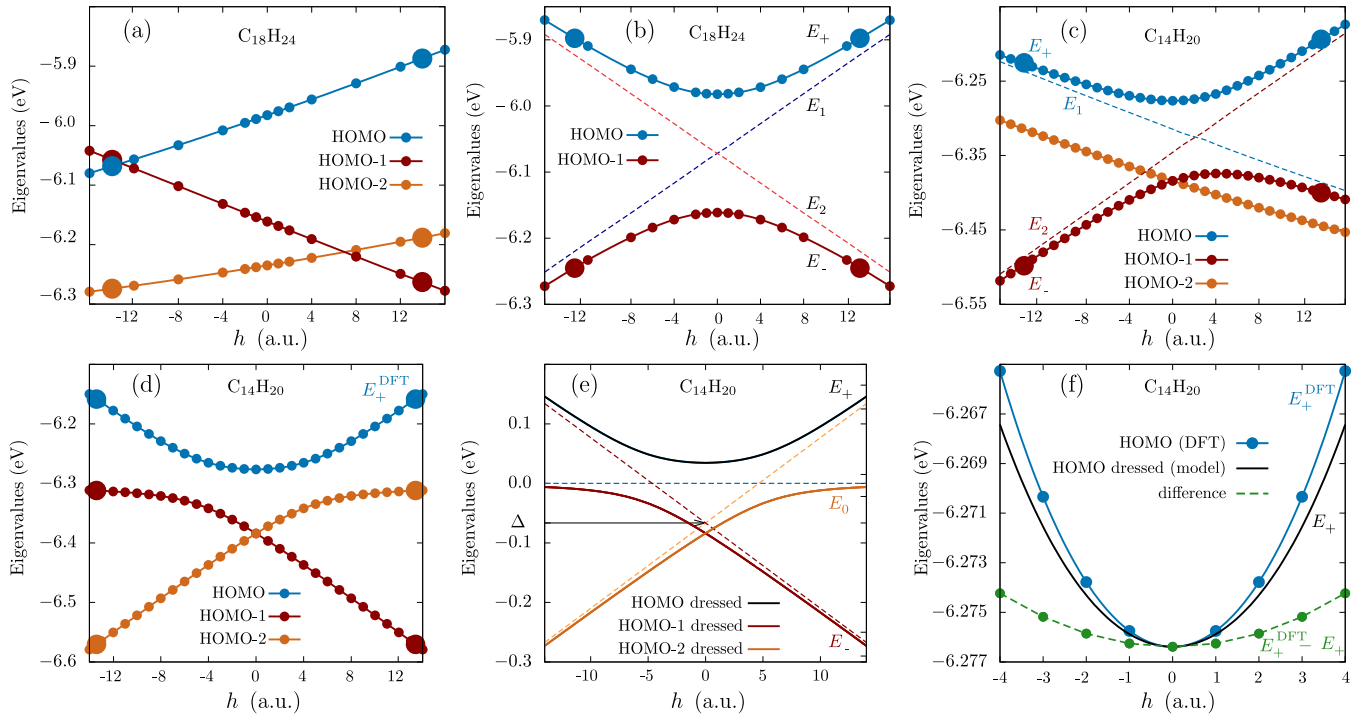

FIG. 1. Eigenvalues as a function of the frozen-phonon displacements h for (a) $C_{18}H_{24}$ for a phonon with a wave number of 1131 cm^{-1}, (b) $C_{18}H_{24}$ for a phonon with a wave number of 1256 cm^{-1}, (c) $C_{14}H_{20}$ for a phonon with a wave number of 1217 cm^{-1}, (d) $C_{14}H_{20}$ for a phonon with a wave number of 1301 cm^{-1}, (e) bare and dressed states extracted from (d) (see text), and (f) HOMO from DFT [as in (d)] and HOMO from the model [as in (e)] and difference between the two (dashed line). The large dots in (a)–(d) correspond to the displacements suggested in Ref. [15] (i.e., $\mathbf{x}_\pm^\nu = \mathbf{x}_0 \pm \mathbf{U}^\nu/\sqrt{\omega_\nu}$).

of the second derivative, to follow the electronic state [HOMO in Fig. 1(a)] across the crossing and avoid mixing different electronic states.

In order to recognize a state anticrossing (or crossing) situation we propose the following procedure. We first perform self-consistent density functional theory (DFT) calculations with the undisplaced nuclear position $\mathbf{x}_0$ and the displacement $\mathbf{x}_0 \pm h\mathbf{U}^\nu$ to obtain the electronic eigenvalues $E_n(\mathbf{x}_0)$ and $E_n(\mathbf{x}_0 \pm h\mathbf{U}^\nu)$. A small displacement with $h \approx 2$ a.u. is used. Next, the overlap between undisplaced $|u\rangle$ and displaced $|d\rangle$ states $\chi = |\langle u|d\rangle|^2$ is calculated. When the overlap is close to 1.0 (e.g., > 0.995 for $h = 2$ in our case [36]), we calculate the renormalization according to Eq. (5). Otherwise, we recalculate the electronic eigenvalues with different displacements $h = \pm 1,\ \pm 3,\ \pm 4, \ldots$. By visual inspection, we identify the situation [Fig. 1(a)–1(c), or 1(d)] and apply the corresponding correction method (as explained below).

C. Crossing of two states

If there is a crossing, as displayed in Fig. 1(a), we must make sure to use eigenvalues in Eq. (5) that belong to the same branch to calculate the curvature of E_n vs h in order to calculate the correct renormalization. For example, if we want to find the renormalization of HOMO-1 in Fig. 1(a) (red line) and we use $h = +12$, we must no longer use the second-highest occupied eigenvalue, but the third-highest one, which is the one which corresponds to a smooth E_n-vs-h curve (that is, we need to *follow* the eigenvalue). The appropriate eigenvalue can also be found from the overlap of wave functions χ (see the Supplemental Material [30] and tutorial [37]).

D. Avoided crossing of two states

We map the simple state anticrossing situation in Fig. 1(b) and the asymmetric anticrossing in Fig. 1(c) to the equation

$$\left| \begin{pmatrix} E_1 & g \\ g & E_2 \end{pmatrix} - \mathbb{I} \cdot E_\pm \right| = 0, \tag{7}$$

where $\mathbb{I}$ is the identity matrix, $E_\pm$ are the eigenvalues obtained from DFT calculations (*dressed eigenvalues*), and $E_{1,2}$ are the so-called bare states. $E_\pm$ include the ZPR with contributions from the unwanted anticrossing effect. We therefore extract the ZPR effect from Eq. (7) as

$$E_{\frac{1}{2}} = \frac{E_+ + E_- \pm \sqrt{(E_+ - E_-)^2 - 4g^2}}{2}. \tag{8}$$

The coupling parameter g is half the minimal distance between the dressed curves (E_+ and E_-) and is obtained from a polynomial fit to the DFT eigenvalues. By solving Eq. (8), we fit $E_{1,2}$ vs h to a parabola and extract its second derivative (curvature) ζ. The frozen-phonon ZPR is then calculated via the relation $\Delta E_n^\nu(0) = \zeta/(2\omega_\nu)$ [see Eq. (5)]. In Figs. 1(b) and 1(c), we show the calculated bare eigenvalues (dashed lines) as well as the dressed eigenvalues from DFT (circles). The solid lines are polynomial fits to the data points. Note that in Fig. 1(b) the curvature of $E_{1,2}$ are very small, leading to a small contribution to the ZPR (0.3 meV in this case).

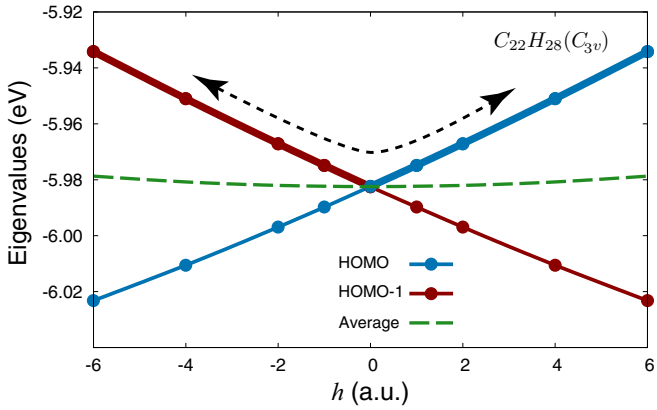

FIG. 2. Degenerate HOMO of $C_{22}H_{28}$ with C_{3v} symmetry as a function of the displacement parameter h for a phonon with a wave number of 1336 cm^{-1}.

E. Avoided crossing of three states

The Hamiltonian describing the anticrossing situation [38] in Fig. 1(d) is given by

$$\hat{H} = \begin{pmatrix} \Delta + ah & g & g_3 \\ g & 0 & g \\ g_3 & g & \Delta - ah \end{pmatrix}. \quad (9)$$

The values of a and Δ used in Eq. (9) are obtained from DFT calculations in the large h limit [via asymptotes; dashed lines in Fig. 1(e)], and g is the minimal distance between the HOMO and the HOMO-1 state from DFT calculations [solid lines in Fig. 1(d)]. The numerical solution of Eq. (9) is shown in Fig. 1(e). In the case of $h = 0$, the electronic eigenvalues can be analytically written as

$$E_+(h=0) = \tfrac{1}{2}(\Delta + g_3 + \sqrt{8g^2 + (\Delta + g_3)^2}), \quad (10a)$$

$$E_0(h=0) = \tfrac{1}{2}(\Delta + g_3 - \sqrt{8g^2 + (\Delta + g_3)^2}), \quad (10b)$$

$$E_-(h=0) = \Delta - g_3. \quad (10c)$$

The requirement of a crossing of states E_- and E_0 at $h = 0$, which is dictated by the symmetry, leads to an analytic solution for the coupling g_3:

$$g_3 = \tfrac{1}{2}(\Delta + \sqrt{\Delta^2 + 4g^2}). \quad (11)$$

Once the values of $E_\pm(h)$ are obtained, we extract its concavity ζ and calculate the frozen-phonon renormalization using $\Delta E_n^\nu(0) = \zeta/(2\omega_\nu)$.

In Fig. 1(f) the dressed eigenvalues of the anticrossing model E_+ are shown by the solid black line, and the DFT eigenvalues are shown as blue dots E_+^{DFT}. The difference between the two is shown by the dashed green line. From this difference we extract the second derivative ζ. In the analyzed example, the uncorrected (corrected) renormalization is 56.2 (11.8) meV.

F. Treatment of degenerate states

Among the 17 structures analyzed in this paper, 3 of them have a twofold HOMO, and 8 of them have a threefold HOMO. In Fig. 2 we show the twofold HOMO of $C_{22}H_{28}$ with C_{3v} symmetry as a function of the displacement parameter h (see Figs. S10 and S11 in the Supplemental Material for further examples [30]). In the case of degeneracy, one possible approach is to assume that all the degenerate states will contribute equally in the light emission or absorption process. This leads to the averaging of the different contributions, as performed previously [39–43] as well as in this work (see also Sec. II B of the Supplemental Material [30]). Importantly, using the averaging procedure, there is no correction needed from degenerate perturbation theory to the perturbation theory of AHC (the equations in Sec. IV are valid) or to the frozen-phonon approach.

Going beyond the averaging procedure, i.e., occupying only or mainly the band gap state shown by thick lines (along the dashed arrow) in Fig. 2, is not trivial. It is conceivable that the system will undergo a dynamical transition between the two branches (thick lines), which may be taken into account in Floquet theory [44], where a dynamically created gap opens up. On the other hand, the dynamics of the coupled system with a corresponding (mixed) band edge state is readily obtained by molecular dynamics (MD) [43,45,46]. Missing pieces in MD are excitonic effects. In the excitonic picture, the ground state exciton has contributions from both HOMO states (HOMO and HOMO-1 in Fig. 2), and the exciton manifold can be thermally occupied to match the experimental situation. Such methodological developments would be interesting to pursue.

Recently, the addition of a term in the AHC model as well as in the FP approach was suggested for the case of degeneracies [19]. The use of degenerate perturbation theory and the assumption that the band gap states undergo the transition indicated by the dashed arrow in Fig. 2 with a sudden change in wave function symmetry at $h = 0$ lead to a very large nonvanishing linear correction term that we decided not to include in our results. A discussion of this approach is given in the Supplemental Material [30].

III. STRUCTURES UNDER INVESTIGATION

We investigated 16 diamondoids and urotropine ($C_6H_{12}N_4$, where four methine groups of adamantane are replaced by nitrogen), as shown in Fig. 3 (atomic positions can be found in [37]). Diamondoids are ideal candidates to study ZPR. These small fragments of diamond passivated with hydrogen present a strong ZPR [9,10,23] and can be simulated *ab initio* with an affordable computational burden. Diamondoids present many forms, like those of a cube, a cane, a disk, or a pyramid [47]. Three of the smallest diamondoids, adamantane ($C_{10}H_{16}$), diamantane ($C_{14}H_{20}$) and triamantane ($C_{18}H_{24}$), usually called *lower diamondoids*, have no isomers, in contrast to larger *higher diamondoids*. The systems that we analyze in this paper have been the object of *ab initio* calculations in the past to different extents. On the one hand, the lower diamondoids are the object of intense computational [9,10,23,48] and experimental [49,50] research. On the other hand, higher diamondoids have been the object of fewer experiments [51] and several computational studies [43,48,52–60].

IV. FURTHER METHODS

We use the QUANTUM ESPRESSO (version 5.3.0) package [61] with the LDA [62] exchange correlation and

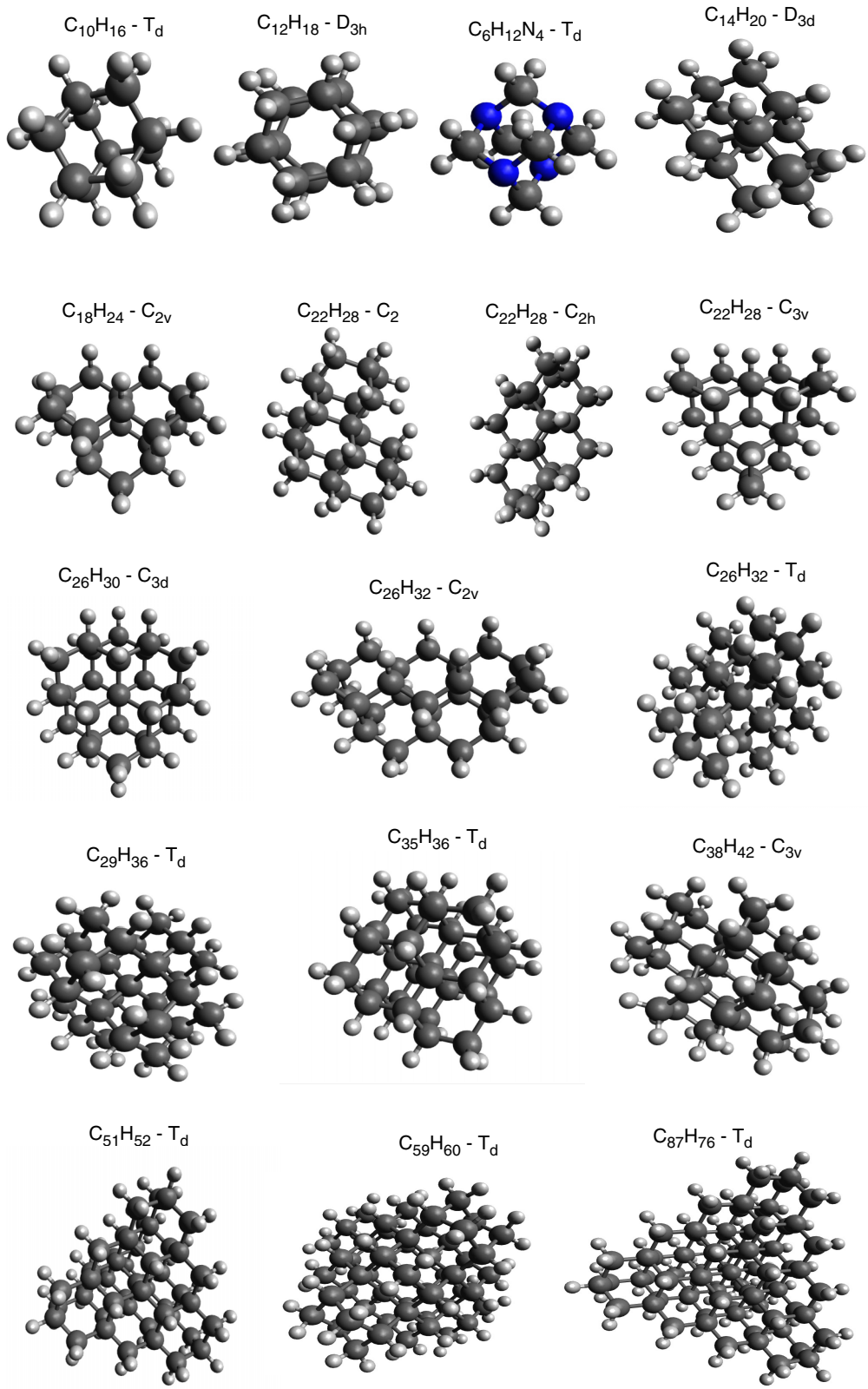

FIG. 3. Nanostructures investigated in this paper (16 diamondoids and urotropine). $C_{10}H_{16}$, $C_{12}H_{18}$, $C_{14}H_{20}$, $C_{18}H_{24}$, $C_{22}H_{28}$, $C_{26}H_{32}$, $C_{26}H_{30}$, and $C_6H_{12}N_4$ are commonly known as adamantane, iceane, diamantane, triamantane, tetramantane, pentamantane, hexamantane, and urotropine, respectively.

Baroni-del Corso (VBC) pseudopotentials [63] as well as the GGA Perdew-Burke-Ernzerhof (PBE) [64] exchange correlation with HGH pseudopotentials [65] and the B3LYP [66,67] exchange correlation with Hartwigsen-Goedecker-Hutter (HGH) pseudopotentials [65]. For the B3LYP calculations we used the relaxed geometries and normal modes obtained at the GGA-PBE level. The plane-wave cutoffs were 30 Ry for GGA and LDA and 60 Ry for B3LYP. The forces were converged to 10^{-6} Ry/bohr. The simulation cells were cubic, with edges of 35 Å for systems up to 18 carbons, 36 Å for systems with 22 to 35 carbons, 37 Å for systems with 38 and 51 carbons, and 38 Å for the largest diamondoid. In the Supplemental Material [30] we present an example of the renormalization energy as a function of the size of the simulation cell and provide in [37] a downloadable step-by-step description and necessary codes.

In Sec. V, we compare our results with the standard [16] AHC theory [5,68–70]. The AHC approach is based on the Green's function many-body perturbation theory, and the renormalizations are calculated as electronic self-energies. In this theory, such self-energies consist of two terms: the Fan self-energy and the DW self-energy. The former ($\Sigma^{\rm Fan}$) corresponds to linear electron-phonon couplings g treated in second-order perturbation theory [20,71], while the latter ($\Sigma^{\rm DW}$) corresponds to quadratic couplings $g^{\rm DW}$ treated in first-order perturbation theory [5,21]. Within the framework of that theory the renormalization of electronic eigenvalues is not directly calculated from finite difference in the electronic eigenvalues—as done in our frozen-phonon approach—but from finite-difference variations of the self-consistent potential. For their calculation we follow Ref. [14]. The AHC results that we present in Table IV below are based on the following equations:

$$\begin{aligned}
\Delta E_n(T) &= \Sigma_n^{\rm Fan}(T) + \Sigma_n^{\rm DW}(T),\\
\Sigma_n^{\rm Fan}(T) &= \sum_{\nu,\ j\neq n} \frac{|g_\nu^{n,j}|^2}{E_n - E_j}\left(2n_\nu^B + 1\right),\\
\Sigma_n^{\rm DW}(T) &= \sum_\nu (g^{\rm DW})_\nu^{n,n}\left(2n_\nu^B + 1\right),\\
g_\nu^{n,j} &= \sum_I \sqrt{\frac{1}{2M_I\,\omega_\nu}}\,\langle j|\,\nabla_I \widehat{H}^0|\,n\rangle\,\mathbf{X}_I^\nu,\\
(g^{\rm DW})_\nu^{n,n} &= \sum_{IJ} \frac{\left(\mathbf{X}_I^\nu\right)^\dagger\,\langle n\mid \nabla_I\nabla_J\,\widehat{H}^0\mid n\rangle\,\mathbf{X}_J^\nu}{4\sqrt{M_I M_J}\,\omega_\nu},
\end{aligned} \tag{12}$$

where E_n and E_j are the unperturbed electronic eigenvalues, ω_ν are the phonon frequencies (with $\nu = 7,\ldots,3\,N_{\rm at}$, where $N_{\rm at}$ is the number of atoms), and n_ν^B is the Bose distribution. The indices n and j correspond to electronic eigenvalues, with $|n\rangle$ and $|j\rangle$ being the corresponding orbitals, and I and J are the atom indices. $\widehat{H}^0$ is the unperturbed Hamiltonian (evaluated at relaxed nuclear positions), whose first and second derivatives with respect to the nuclear displacements determine the couplings. The summation in the electronic orbitals [j index in Eq. (12)] includes all the occupied and unoccupied states except $j = n$; in practice the summation is truncated and includes several hundred orbitals [7,9,21] (see the Supplemental Material [30]). Alternatively, one can use projectors to avoid large summations, as explained in Refs. [20,21].

The direct calculation of the Debye-Waller term is numerically heavy because it requires the evaluation of the second derivative of the Hamiltonian with respect to nuclear positions. A simple and efficient manner to calculate part of it is given by the *rigid-ion approximation* [20,22]. This approximation consists of considering that the (Kohn-Sham) potential can be split into a sum of potentials which depend on the individual nuclear (ionic) positions. Under the rigid-ion approximation, the Debye-Waller electron-phonon matrix elements $g^{\rm DW}$ can be calculated using

$$(g^{\rm DW})_\nu^{n,n} = \sum_{\substack{I\alpha\\ I'\alpha'}} \frac{\left(U_{I,\alpha}^\nu U_{I,\alpha'}^\nu + U_{I',\alpha}^\nu U_{I',\alpha'}^\nu\right)}{2\ \omega_\nu} \times \left[\sum_{\substack{j=1\\ j\neq n}}^{\infty} \frac{h^{n,j;\alpha,I} h^{n,j;\alpha',I'}}{E_j - E_n}\right], \tag{13a}$$

$$h^{n,j;\alpha,I} = \sum_\nu M_I\,\sqrt{\omega_\nu}\,U_{I,\alpha}^\nu\,g_\nu^{n,j}. \tag{13b}$$

With this approximation, the Fan and DW terms require only the calculation of $g_\nu^{n,j}$ (e.g., using the δV approach [14]), in addition to the phonon eigenmodes and eigenenergies.

V. RESULTS

A. Our frozen-phonon results

Our results for the renormalization of the HOMO, LUMO, and gaps are summarized in Table I, where we also present the renormalization of the LUMO + 1 of $C_{14}H_{20}$ and $C_{22}H_{28}$ with C_{2h} symmetry because the HOMO/LUMO optical transition is forbidden due to symmetry arguments [23]. For $C_{29}H_{36}$ we employed the geometry from GGA for the calculations with LDA, GGA, and B3LYP.

In Table I the B3LYP results for the largest diamondoids are lacking due to their large computation cost. In Table I we also display (in bold font) the number of *problematic modes* in the calculation of the renormalization of the HOMO state. Note that this number depends on the chosen functional. Since a mode can become problematic when two or more eigenvalues are close in energy, this can well depend on the functional used. For instance, the LDA and GGA may lead to slightly different structural relaxations, and electronic states that are close in energy in the LDA (creating problematic modes) may be sufficiently far at the GGA level so that no (or fewer) problematic modes appear. If the correction for the anticrossings is done properly, we should, however, obtain similar final results for the ZPR.

As shown in Table I (bold numbers), 5 (6 with B3LYP) out of 17 structures present problematic modes and require the appropriate correction. The failure to do so can lead to large errors that will be presented subsequently in detail in Table III.

Moreover, Table I indicates that the renormalizations of the HOMO and LUMO obtained at the GGA and LDA level are very similar. For the hybrid functional B3LYP we obtain similar (to LDA and GGA) renormalizations of the gap

TABLE I. ZPR of the HOMO, LUMO, and gap of diamondoids and urotropine (in meV). The numbers in bold font indicate the number of modes for which a correction due to an anticrossing was necessary; (2x) and (3x) indicate HOMO degeneracies. The LDA results for $C_{59}H_{60}$ are absent because the HOMO and HOMO-1 states are very close in energy using this functional, which requires a very cumbersome correction scheme (many problematic modes).

System (symmetry)	State	GGA	LDA	B3LYP	System (symmetry)	State	GGA	LDA	B3LYP
$C_{10}H_{16}$	HOMO (3x)	162.4	157.3	202.9	$C_{26}H_{32}$	HOMO	200.4	185.7	236.7, **1**
(T_d)	LUMO	−86.6	−105.3	−71.4	(C_{2v})	LUMO	−80.2	−100.8	−59.4
	Gap	−249.0	−262.6	−274.3		Gap	−280.6	−286.5	−296.1
$C_{12}H_{18}$	HOMO (2x)	224.2	202.5	295.7	$C_{26}H_{32}$	HOMO (3x)	136.4	125.6	170.8
(D_{3h})	LUMO	−92.2	−109.9	−73.8	(T_d)	LUMO	−73.7	−97.6	−70.3
	Gap	−316.4	−312.4	−369.5		Gap	−210.1	−223.2	−241.1
$C_{14}H_{20}$	HOMO	268.9, **8**	279.2, **6**	318.3, **8**	$C_{29}H_{36}$	HOMO (3x)	175.2	188.7	187.2
(D_{3d})	LUMO	−91.3	−113.5	−49.3	(T_d)	LUMO	−93.9	−115.0	−72.4
	LUMO+1	−67.9	−87.9	−23.7		Gap	−269.1	−303.7	−259.6
	Gap (H/L)	−360.2	−392.7	−367.6	$C_{35}H_{36}$	HOMO (3x)	127.5	123.4	168.7
	Gap (H/L+1)	−336.8	−367.1	−342.0	(T_d)	LUMO	−95.5	−116.9	−81.5
$C_{18}H_{24}$	HOMO	183.2, **2**	221.4, **2**	239.2, **4**		Gap	−223.0	−240.3	−250.2
(C_{2v})	LUMO	−84.2	−103.7	−57.2	$C_{38}H_{42}$	HOMO	205.7, **4**	228.1, **4**	255.1, **4**
	Gap	−267.4	−325.1	−296.4	(C_{3v})	LUMO	−117.9	−115.9	−75.5
$C_{22}H_{28}$	HOMO	272.4, **22**	234.2, **18**	267.4, **26**		Gap	−323.6	−344.0	−330.6
(C_2)	LUMO	−86.4	−106.9	−59.2	$C_{51}H_{52}$	HOMO (3x)	101.9	97.7	
	Gap	−358.8	−341.1	−326.6	(T_d)	LUMO	−100.6	−92.3	
$C_{22}H_{28}$	HOMO	177.5, **1**	174.0, **1**	239.2, **2**		Gap	−202.5	−190.0	
(C_{2h})	LUMO	−66.5	−89.7	−44.6	$C_{59}H_{60}$	HOMO (3x)	192.8		
	LUMO+1	−80.7	−100.7	−83.6	(T_d)	LUMO	−101.1		
	Gap (H/L)	−244.0	−263.7	−283.8		Gap	−293.9		
	Gap (H/L+1)	−258.2	−274.7	−322.8	$C_{87}H_{76}$	HOMO (3x)	96.6	79.2	
$C_{22}H_{28}$	HOMO (2x)	188.8	181.1	240.6	(T_d)	LUMO	−61.3	−89.9	
(C_{3v})	LUMO	−85.5	−100.5	−58.8		Gap	−157.9	−169.1	
	Gap	−274.3	−281.6	−299.4					
$C_{26}H_{30}$	HOMO (2x)	167.2	159.2	221.2	$C_6H_{12}N_4$	HOMO (3x)	−29.5	−35.4	−11.9
(C_{3d})	LUMO	−73.9	−102.0	−46.2	(T_d)	LUMO	−68.7	−82.3	−50.3
	Gap	−241.1	−261.2	−267.4		Gap	−39.2	−46.9	−38.4

but rather different renormalizations of HOMO and LUMO individually. Quantitatively, the average difference between LDA and B3LYP is −30% for the HOMO and 35% for the LUMO but only 8.6% for the HOMO-LUMO gap. This means that, although B3LYP calculations are desirable, the cheaper LDA and GGA provide satisfactory results in the calculation of gap renormalizations due to ZPR. Note that the B3LYP results can be expected to be rather accurate, as shown in Ref. [72], where the renormalization of the LUMO of C_{60} was calculated using LDA/GGA, B3LYP, and self-consistent *GW*. Using the latter as a reference, the error made by the LDA was about 30%, while the error from B3LYP was only 10%.

In Fig. 4, we show the frozen-phonon renormalizations of the HOMO, LUMO, and HOMO-LUMO gap for the 16 analyzed structures. We can see that the values of the gap renormalizations lie between −158 meV ($C_{87}H_{76}$) and −393 meV ($C_{14}H_{20}$) and are on the same order of magnitude as for bulk diamond: between −320 and −450 meV for the direct gap [73] and −340 and −370 meV for the indirect gap [74,75]. We notice that the renormalizations of the HOMO are always positive (for diamondoids, not including urotropine) and the renormalizations of the LUMO are always negative, which is the usual behavior [8,23]. In addition, we notice that for diamondoids the magnitude of the HOMO renormalization is always larger than that of the LUMO renormalization and that the values of the LUMO renormalizations are very similar for all the analyzed diamondoids (about −100 meV for LDA and GGA functionals and about −70 meV for B3LYP). The latter property is due to the fact that the LUMO states are localized just outside the diamondoids (surface-bound states) due to the negative electron affinity [52].

In an attempt to understand the general trends, we differentiate the effect of the size (number of carbon atoms) and the effect of the geometry (symmetry) of the structures. From the comparison of the three structures with 22 carbon atoms we can see that the shape/symmetry effect is not negligible, with differences of 10% in the ZPR. The results show the overall trend that the ZPR decreases with increasing size in a nonmonotonous way with fluctuations we could interpret as shape/symmetry effects. The structure $C_{10}H_{16}$ lies somewhat outside this trend. We can tentatively understand this "outlier" when we look at the two $C_{26}H_{32}$ structures and notice that the one with T_d symmetry has lower ZPR. The $C_{10}H_{16}$ structure has T_d symmetry as well, and we would therefore expect it to have a lower ZPR. This symmetry/shape effect is larger than

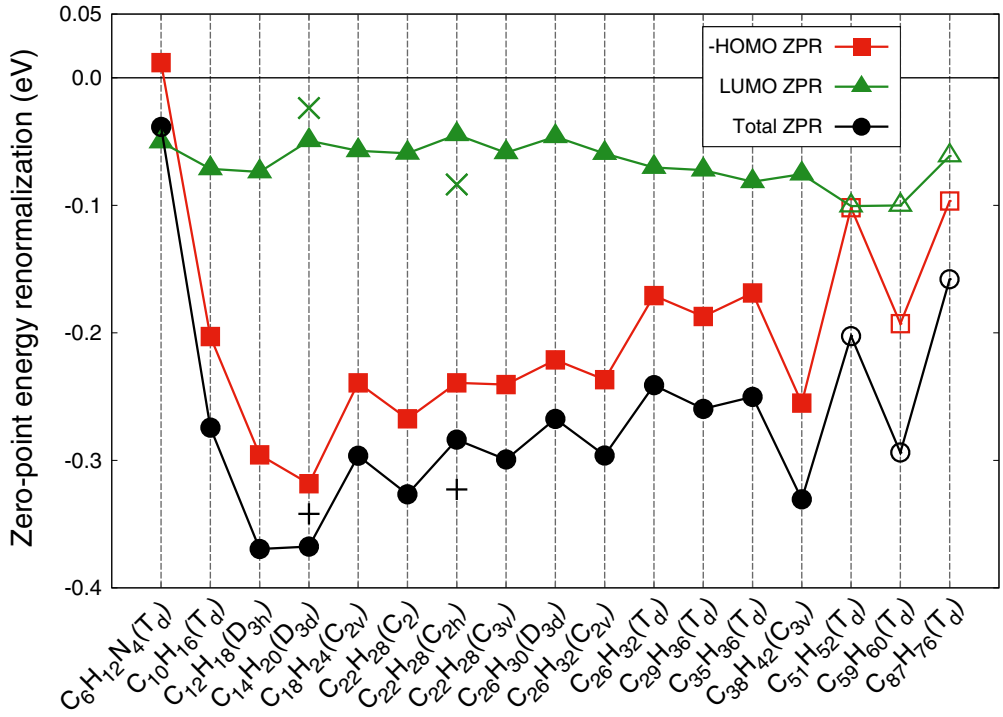

FIG. 4. ZPR of urotropine and diamondoids. The HOMO renormalization is shown with opposite sign. Solid symbols indicate calculations performed with the B3LYP exchange-correlation functional; open symbols correspond to the GGA-PBE functional. The crosses indicate renormalization of the LUMO + 1, and the plus signs are the HOMO/LUMO + 1 gap.

for other structures because of the small size and molecular character of $C_{10}H_{16}$.

Urotropine, which in contrast to the diamondoids contains nitrogen atoms, shows qualitatively different renormalizations. We can understand this difference from the electronic structure of the HOMO. In urotropine, the HOMO is composed of the lone pairs and is very different and much more delocalized than, e.g., in the case of adamantane, in which the HOMO is well localized inside the structure. We present the HOMO states of adamantane and urotropine at the bottom of Fig. 5. The ZPR in urotropine is therefore similar for the HOMO (lone pair states [76]) and the LUMO (surface-bound state [52]).

B. Comparison to available ab initio results

In Table II we compare our results to available *ab initio* calculations [10,43,48] (we are not aware of experimental results). In Ref. [10] the ZPR was calculated as the summation for vibronic modes $\sum_\nu(\hbar/2)(\omega_{s,\nu}-\omega_{0,\nu})$, where $\omega_{0,\nu}$ and $\omega_{s,\nu}$ are the phonon frequencies for the ground state and the excited singlet state (index s). In Ref. [48] the ZPR was calculated using the standard AHC theory (as presented above in this paper), using DFT (GGA) and G_0W_0. For the comparison, we assume that the results for $C_{22}H_{28}$ and $C_{26}H_{32}$ presented in [48] correspond to the C_{2h} and T_d symmetries, respectively. The calculations of Ref. [43] were based on *ab initio* molecular dynamics simulations.

The general agreement between the different theoretical results is rather good for most of the structures. The differences between our results and the AHC results can be partially explained by the NRIA DW contribution which is intrinsically included in our FP but not in the AHC model. However, for adamantane the disagreement with Ref. [48] is rather large (−430 vs −249 meV) and may not be attributed to the NRIA DW contribution alone, so we remain uncertain about the reasons for the large discrepancy. Our own AHC calculations (see also Sec. V E) for this structure yield −273 meV, which is, again, in good agreement with the FP results. It is also interesting to note that G_0W_0 [48] changed the results in a significant manner, reducing the magnitude of ZPR by about 20% (compared to the PBE results), while B3LYP made a rather moderate impact of around 7% in the opposite direction, increasing the magnitude of ZPR.

C. Temperature dependence of the band gap and comparison with bulk diamond

In Fig. 6 we plot the temperature dependence of the band gap renormalization (calculated at the LDA level) of the different diamondoids and diamond. Note that our calculations do not include changes in the bond lengths (lattice thermal expansion), which contributes to a minor band gap renormalization [15,77]. Since we have no information about experimental results for ZPR in diamondoids, we plot the experimental results for bulk diamond from Ref. [73] (solid triangles and circles; two different data sets are presented in this paper) for the direct band gap and Ref. [74] for the indirect band gap (solid squares). These experiments estimated ZPRs of 0.32 and 0.45 eV for Ref. [73] and 0.37 eV for Ref. [74],

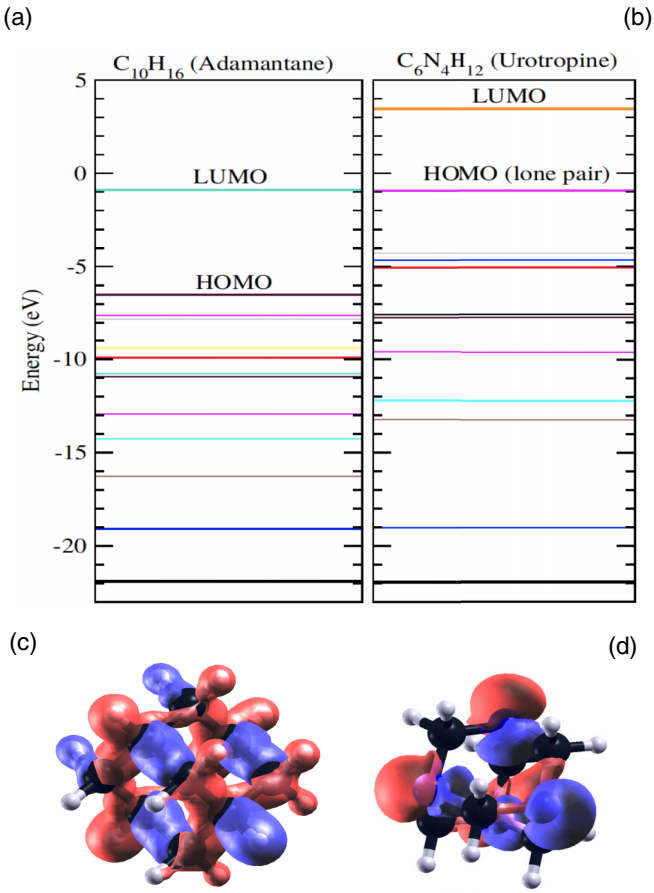

FIG. 5. The electronic states of (a) adamantane ($C_{10}H_{16}$) and (b) urotropine ($C_6N_4H_{12}$) obtained from DFT-LDA calculations are arbitrarily aligned at the lowest eigenvalue. The square of the HOMO wave function is shown as an isosurface in (c) for adamantane and in (d) for urotropine.

and these values are used in the plot. The ZPRs of the diamondoids are in the same energy range as that of diamond, which has very large values compared to other materials [75]. The temperature dependence seems less pronounced than in diamond for almost all the structures, except for $C_{14}H_{20}$ and $C_{38}H_{42}$, in which it is very similar to that of diamond.

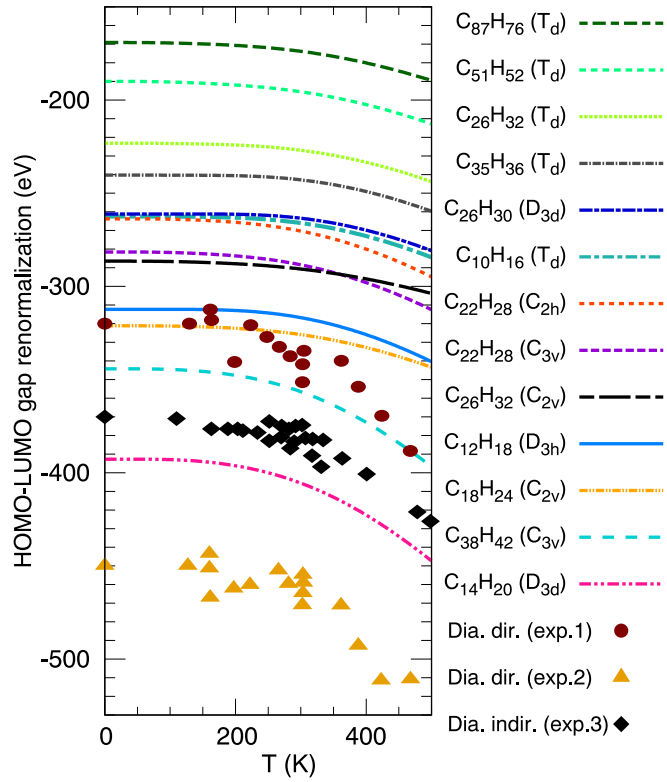

FIG. 6. Temperature dependence of the HOMO-LUMO gap (LDA), neglecting lattice expansion effects. Experimental results for bulk diamond are taken from Ref. [73] (exp. 1 and exp. 2, direct gap) and Ref. [74] (exp. 3, indirect gap).

D. Magnitude of the correction

In Table III we present the magnitude of the applied correction for the five structures affected. The 12 other structures show no anticrossing and therefore require no correction. Only the HOMO was affected for our structures; since the LUMO is energetically well separated from the LUMO + 1, the anticrossing situation did not occur. The HOMO is, for all the structures presented, nondegenerate (onefold). All the calculations in Table III were performed at the B3LYP level. The corrections can obviously be very large, especially for $C_{22}H_{28}$ (C_2), for which we corrected a total of 29 frozen phonon modes and obtained a correction term that surpasses the ZPR itself (26 modes with anticrossing, 3 modes with

TABLE II. Comparison between different *ab initio* results for the ZPR of the band gap. In the first column in the parentheses we give the symmetry (Sym.) and degeneracy (Deg.) of the HOMO, and the asterisk indicates structures which have undergone a correction (Corr.) due to anticrossing(s). Calculations were performed at the LDA level with a 30 Ry energy cutoff.

Structure (Sym., Deg., Corr.)	Ref. [10] (Franck-Condon)	Ref. [43] MD center	Ref. [48] (AHC, PBE)	This paper (AHC, PZ)	This paper (FP, PBE)	Ref. [48] (AHC, G_0W_0)	This paper (FP, B3LYP)
$C_{10}H_{16}$ (T_d, 3x)	−320		−430	−273	−249	−380	−274
$C_{14}H_{20}$ (D_{3d}, 1x, *)	−270		−340		−360	−280	−367
$C_{18}H_{24}$ (C_{2v}, 1x, *)	−250		−310		−267	−260	−296
$C_{22}H_{28}$ (C_{2h}, 1x, *)			−290		−244	−190	−284
$C_{26}H_{30}$ (C_{3d}, 2x)			−290		−241	−240	−267
$C_{26}H_{32}$ (T_d, 3x)		−220	−300		−210	−250	−241
$C_{87}H_{76}$ (T_d, 3x)			−220		−158	−190	

TABLE III. Corrections (Corr.) due to crossing (cross.) and anticrossing (AC) effects. The last column gives the anticrossing correction as a percentage of the final value of the HOMO ZPR. The calculations are done at the B3LYP level of DFT. The HOMO of all the structures is nondegenerate.

Structure symmetry	Corr. due to AC (meV)	Corr. due to cross. (meV)	Corrected HOMO ZPR (meV)	AC Corr. (%)
$C_{14}H_{20}$ (D_{3d})	−244	0	318	−77
$C_{18}H_{24}$ (C_{2v})	−207	0	239	−87
$C_{22}H_{28}$ (C_2)	−495	−280	267	−185
$C_{22}H_{28}$ (C_{2h})	−88	0	239	−37
$C_{38}H_{42}$ (C_{3v})	−11	0	255	−4

crossing, B3LYP). Due to the small displacement parameter used ($h = 2$), only one structure underwent a crossing. This is an advantage of using small displacement parameters that lead to very few cases of state crossing.

E. Comparison of our corrected frozen-phonon results with AHC theory

In Table IV we present the results from our corrected frozen-phonon approach and from the AHC perturbation theory for a selection of diamondoids. All calculations were performed with the Perdew and Zunger exchange correlation functional and with VBC pseudopotentials [63], a plane-wave cutoff of 30 Ry, and a displacement parameter of $h = 2$. In the AHC calculations we use the finite-difference δV approach to calculate the matrix elements, following Ref. [14]. For the calculation of the HOMO renormalizations, we used 400 orbitals [index j in Eqs. (12) and (13a)], which seems to give converged results [30]. For the LUMOs, a much larger number of orbitals was necessary. For adamantane and $C_{26}H_{32}$ with C_{2v} symmetry we went up to 2000 orbitals to achieve convergence [30]. A Sternheimer projection formalism [21] was not used but would be advisable and may solve this problem. Since the comparison between our FP method and the AHC model is not the main objective of our paper, we did not perform the numerically demanding calculations for the other diamondoids and have no reliable results to present for the LUMO renormalization of $C_{22}H_{28}$ (C_{2h}) and $C_{14}H_{20}$ (D_{3d}) (entries marked with a dash in Table IV). The renormalization provided by the FP approach includes the Fan and Debye-Waller (both diagonal and nondiagonal, also called *non-rigid-ion*) renormalizations from the AHC formalism [20,21]. The Debye-Waller self-energy Σ^{DW} in the AHC approach [calculated using Eq. (13)] lacks a non-rigid-ion part [20]. Therefore, the renormalization calculated using this standard form of the AHC theory [16] presents two drawbacks: (i) a high number of orbitals [maximum j in Eqs. (12) and (13a)] is commonly necessary for appropriate accuracy; (ii) the non-rigid-ion part of the self-energy is missing. Both drawbacks are avoided by using the frozen-phonon method that we present in this paper. From Table IV we see that the NRIA-DW self-energies, which correspond mainly to the difference between the FP and AHC results, are negative, with values between −23 and −86 meV, which is on the same order of magnitude as for the diatomic molecules presented in Ref. [21]. This rather large difference reinforces the usefulness of the frozen-phonon approach.

TABLE IV. ZPR of the HOMO and LUMO of diamondoids obtained from our frozen-phonon method (FP, LDA, 30 Ry cutoff) and from the Allen-Heine-Cardona (AHC) theory (Fan and rigid-ion Debye-Waller self-energies) and the difference between the two. For the entries marked with a dash (—) we have no reliable converged results. All values are in meV.

Structure	HOMO			LUMO		
(symmetry)	FP	AHC	Diff.	FP	AHC	Diff.
$C_{10}H_{16}$ (T_d, 3x)	157	198	−41	−105	−75	−30
$C_{14}H_{20}$ (D_{3d}, 1x)	279	256	−23	−114	–	–
$C_{22}H_{28}$ (C_{2h}, 1x)	174	259	−85	−90	–	–
$C_{22}H_{28}$ (C_{3v}, 2x)	181	195	−14	−101	–	–
$C_{26}H_{32}$ (C_{2v}, 1x)	186	272	−86	−101	−65	−36
$C_{26}H_{32}$ (T_d, 3x)	126	166	−41	−98	–	–

VI. CONCLUSION

We have introduced a method to perform accurate frozen-phonon calculations of the ZPR when eigenstates of the appropriate symmetry are energetically close to the HOMO or LUMO so that an electronic coupling—evidenced by an anticrossing—overshadows the electron-phonon coupling. This procedure is certainly more laborious than the original procedure [15] since it requires a wave function projection to identify the problematic cases and a subsequent case-by-case correction of the specific modes. However, since it seems that relatively few modes (at least for most of the investigated structures) require postprocessing, the method remains reasonable and competitive. We provide in [37] a complete step-by-step description as well as the necessary codes, which should facilitate further use of the approach.

The application of our method to the ZPR of 16 diamondoids and one modified diamondoid (urotropine) shows that the correction is necessary for 5 (6 with B3LYP) out of the 17 structures, with changes in the ZPR up to 185% (for $C_{22}H_{28}$ with C_2 symmetry). Generally, we confirmed rather strong gap renormalizations for the diamondoids (170 to 370 meV) and predicted a smaller renormalization for urotropine (38 meV). The LDA and GGA results for the band gap renormalizations lie close to those obtained with B3LYP, although the individual HOMO/LUMO results differ by up to 35%.

ACKNOWLEDGMENTS

Most computations were performed on the HPC cluster of the Regional Computing Center of Universität Hamburg. We thank N. Drummond and F. Marsusi for providing the structure of $C_{87}H_{76}$ and Dr. H. Stüben for valuable help and advice. This work is supported by the Cluster of Excellence "CUI: Advanced Imaging of Matter" of the Deutsche Forschungsgemeinschaft (DFG), EXC 2056, Project ID No. 390715994, and DFG Project No. BE 4292/4, "Resonant Raman spectroscopy as tool to investigate colloidal semiconductor nanocrystals."

[1] H. Fröhlich, Electrons in lattice fields, Adv. Phys. **3**, 325 (1954).

[2] T. Holstein, Studies of polaron motion. 1. The molecular-crystal model, Ann. Phys. (NY) **8**, 325 (1959); Studies of polaron motion. 2. The small polaron, **8**, 343 (1959).

[3] S. Engelsberg and J. R. Schrieffer, Coupled electron-phonon system, Phys. Rev. **131**, 993 (1963).

[4] L. Hedin and S. Lundqvist, Effects of electron-electron and electron-phonon interactions on the one-electron states of solids, Solid State Phys. **23**, 1 (1970).

[5] P. B. Allen and V. Heine, Theory of the temperature dependence of electronic band structures, J. Phys. C **9**, 2305 (1976).

[6] F. Giustino, Electron-phonon interactions from first principles, Rev. Mod. Phys. **89**, 015003 (2017).

[7] F. Giustino, S. G. Louie, and M. L. Cohen, Electron-Phonon Renormalization of the Direct Band Gap of Diamond, Phys. Rev. Lett. **105**, 265501 (2010).

[8] G. Antonius, S. Poncé, P. Boulanger, M. Côté, and X. Gonze, Many-Body Effects on the Zero-Point Renormalization of the Band Structure, Phys. Rev. Lett. **112**, 215501 (2014).

[9] A. Gali, T. Demján, M. Vörös, G. Thiering, E. Cannuccia, and A. Marini, Electron-vibration coupling induced renormalization in the photoemission spectrum of diamondoids, Nat. Commun. **7**, 11327 (2016).

[10] C. E. Patrick and F. Giustino, Quantum nuclear dynamics in the photophysics of diamondoids, Nat. Commun. **4**, 2006 (2013).

[11] A. Marini, *Ab Initio* Finite-Temperature Excitons, Phys. Rev. Lett. **101**, 106405 (2008).

[12] M. M. Dacorogna, M. L. Cohen, and P. K. Lam, Self-Consistent Calculation of the **q** Dependence of the Electron-Phonon Coupling in Aluminum, Phys. Rev. Lett. **55**, 837 (1985).

[13] S. Y. Savrasov, D. Y. Savrasov, and O. K. Andersen, Linear-Response Calculations of Electron-Phonon Interactions, Phys. Rev. Lett. **72**, 372 (1994).

[14] P. Han and G. Bester, First-principles calculation of the electron-phonon interaction in semiconductor nanoclusters, Phys. Rev. B **85**, 235422 (2012).

[15] R. B. Capaz, C. D. Spataru, P. Tangney, M. L. Cohen, and S. G. Louie, Temperature Dependence of the Band Gap of Semiconducting Carbon Nanotubes, Phys. Rev. Lett. **94**, 036801 (2005).

[16] Authors citing the Allen-Heine-Cardona work usually make several approximations in their calculations, including (i) calculating the Debye-Waller self-energy using the rigid-ion approximation (also known as *non-diagonal Debye-Waller*), (ii) neglecting the Fermi-Dirac distribution function in the equations of the Fan self-energy Σ^{Fan}, (iii) calculating self-energies through summations including many empty states (instead of using, e.g., a Sternheimer projector, as done, e.g., in [20]), and (iv) calculating renormalizations in *one shot* (i.e., not following self-consistent calculation procedures for eigenvalues and self-energies). This is what we mean when we mention *standard* Allen-Heine-Cardona theory.

[17] P. B. Allen and M. Cardona, Theory of the temperature dependence of the direct gap of germanium, Phys. Rev. B **23**, 1495 (1981).

[18] A. Molina-Sánchez, M. Palummo, A. Marini, and L. Wirtz, Temperature-dependent excitonic effects in the optical properties of single-layer MoS_2, Phys. Rev. B **93**, 155435 (2016).

[19] M. Zacharias and F. Kelires, Quantum confinement of electron–phonon coupling in graphene quantum dots, J. Phys. Chem. Lett. **12**, 9940 (2021).

[20] S. Poncé, G. Antonius, Y. Gillet, P. Boulanger, J. Laflamme Janssen, A. Marini, M. Côté, and X. Gonze, Temperature dependence of electronic eigenenergies in the adiabatic harmonic approximation, Phys. Rev. B **90**, 214304 (2014).

[21] X. Gonze, P. Boulanger, and M. Côté, Theoretical approaches to the temperature and zero-point motion effects on the electronic band structure, Ann. Phys. (Berlin, Ger.) **523**, 168 (2011).

[22] S. Poncé, Y. Gillet, J. Laflamme Janssen, A. Marini, M. Verstraete, and X. Gonze, Temperature dependence of the electronic structure of semiconductors and insulators, J. Chem. Phys. **143**, 102813 (2015).

[23] P. Han and G. Bester, Band gap renormalization of diamondoids: Vibrational coupling and excitonic effects, New J. Phys. **18**, 113052 (2016).

[24] B. Monserrat and R. J. Needs, Comparing electron-phonon coupling strength in diamond, silicon, and silicon carbide: First-principles study, Phys. Rev. B **89**, 214304 (2014).

[25] E. A. Engel, B. Monserrat, and R. J. Needs, Vibrational renormalisation of the electronic band gap in hexagonal and cubic ice, J. Chem. Phys. **143**, 244708 (2015).

[26] B. Monserrat, E. A. Engel, and R. J. Needs, Giant electron-phonon interactions in molecular crystals and the importance of nonquadratic coupling, Phys. Rev. B **92**, 140302(R) (2015).

[27] J. H. Lloyd-Williams and B. Monserrat, Lattice dynamics and electron-phonon coupling calculations using nondiagonal supercells, Phys. Rev. B **92**, 184301 (2015).

[28] B. Monserrat, Vibrational averages along thermal lines, Phys. Rev. B **93**, 014302 (2016).

[29] M. Zacharias and F. Giustino, One-shot calculation of temperature-dependent optical spectra and phonon-induced band-gap renormalization, Phys. Rev. B **94**, 075125 (2016).

[30] See Supplemental Material at http://link.aps.org/supplemental/10.1103/PhysRevB.108.125403 for data, figures and explanations which are complementary to the information presented in the main paper.

[31] P. K. Lam and M. L. Cohen, *Ab initio* calculation of the static structural properties of Al, Phys. Rev. B **24**, 4224 (1981).

[32] S. B. Cronin, Y. Yin, A. Walsh, R. B. Capaz, A. Stolyarov, P. Tangney, M. L. Cohen, S. G. Louie, A. K. Swan, M. S. Ünlü, B. B. Goldberg, and M. Tinkham, Temperature Dependence of the Optical Transition Energies of Carbon Nanotubes: The Role of Electron-Phonon Coupling and Thermal Expansion, Phys. Rev. Lett. **96**, 127403 (2006).

[33] C. E. Patrick and F. Giustino, Unified theory of electron and phonon renormalization and phonon-assisted optical absorption, J. Phys.: Condens. Matter **26**, 365503 (2014).

[34] P. Han and G. Bester, Large nuclear zero-point motion effect in semiconductor nanoclusters, Phys. Rev. B **88**, 165311 (2013).

[35] D. Karaiskaj, C. Engtrakul, T. McDonald, M. J. Heben, and A. Mascarenhas, Intrinsic and Extrinsic Effects in the Temperature-Dependent Photoluminescence of Semiconducting Carbon Nanotubes, Phys. Rev. Lett. **96**, 106805 (2006).

[36] This threshold was heuristically determined from our calculations with diamondoids. See the Supplemental Material [30] for further remarks on the overlap.

[37] https://www.chemie.uni-hamburg.de/institute/pc/arbeitsgruppen/bester/downloads.html.

[38] N. F. Bell, R. F. Sawyer, R. R. Volkas, and Y. Y. Y. Wong, Generation of entangled states and error protection from adiabatic avoided level crossings, Phys. Rev. A **65**, 042328 (2002).

[39] M. Engel, M. Marsman, C. Franchini, and G. Kresse, Electron-phonon interactions using the projector augmented-wave method and Wannier functions, Phys. Rev. B **101**, 184302 (2020).

[40] F. Karsai, M. Engel, E. Flage-Larsen, and G. Kresse, Electron–phonon coupling in semiconductors within the GW approximation, New J. Phys. **20**, 123008 (2018).

[41] A. Miglio, V. Brousseau-Couture, E. Godbout, G. Antonius, Y. Chan, S. G. Louie, M. Côté, M. Giantomassi, and X. Gonze, Predominance of non-adiabatic effects in zero-point renormalization of the electronic band gap, njp Comput. Mater. **6**, 167 (2020).

[42] M. Zacharias, M. Scheffler, and C. Carbogno, Fully anharmonic nonperturbative theory of vibronically renormalized electronic band structures, Phys. Rev. B **102**, 045126 (2020).

[43] A. Kundu, M. Govoni, H. Yang, M. Ceriotti, F. Gygi, and G. Galli, Quantum vibronic effects on the electronic properties of solid and molecular carbon, Phys. Rev. Mater. **5**, L070801 (2021).

[44] H. Hübener, U. De Giovanni, and A. Rubio, Phonon driven Floquet matter, Nano Lett. **18**, 1535 (2018).

[45] R. Ramírez, C. P. Herrero, R. Hernandez, and M. Cardona, Path-integral molecular dynamics simulation of 3*C*-SiC, Phys. Rev. B **77**, 045210 (2008).

[46] R. Ramírez, C. P. Herrero, and R. Hernández, Path-integral molecular dynamics simulation of diamond, Phys. Rev. B **73**, 245202 (2006).

[47] H. Schwertfeger and P. R. Schreinter, Chemie mit nano-juwelen: Diamantoide, Chem. Unserer Zeit **44**, 248 (2010).

[48] R. L. McAvoy, M. Govoni, and G. Galli, Coupling first-principles calculations of electron–electron and electron–phonon scattering, and applications to carbon-based nanostructures, J. Chem. Theory Comput. **14**, 6269 (2018).

[49] T. Zimmermann, R. Richter, A. Knecht, A. A. Fokin, T. V. Koso, L. V. Chernish, P. A. Gunchenko, P. R. Schreiner, T. Möller, and T. Rander, Exploring covalently bonded diamondoid particles with valence photoelectron spectroscopy, J. Chem. Phys. **139**, 084310 (2013).

[50] M. Vörös and A. Gali, Optical absorption of diamond nanocrystals from *ab initio* density-functional calculations, Phys. Rev. B **80**, 161411(R) (2009).

[51] T. Shizuno, H. Miyazoe, K. Saito, S. Stauss, M. Suzuki, T. Sasaki, and K. Terashima, Synthesis of diamondoids by supercritical xenon discharge plasma, Jpn. J. Appl. Phys. **50**, 030207 (2011).

[52] P. Han, D. Antonov, J. Wrachtrup, and G. Bester, Surface-bound states in nanodiamonds, Phys. Rev. B **95**, 195428 (2017).

[53] A. A. Fokin and P. R. Schreiner, Band gap tuning in nanodiamonds: First principle computational studies, Mol. Phys. **107**, 823 (2009).

[54] J. Filik, J. N. Harvey, N. L. Allan, P. W. May, J. E. P. Dahl, S. Liu, and R. M. K. Carlson, Raman spectroscopy of nanocrystalline diamond: An *ab initio* approach, Phys. Rev. B **74**, 035423 (2006).

[55] O. Pirali, M. Vervloet, J. E. Dahl, R. M. K. Carlson, A. G. G. M. Tielens, and J. Oomens, Infrared spectroscopy of diamondoid molecules: New insights into the presence of nanodiamonds in the interstellar medium, Astrophys. J. **661**, 919 (2007).

[56] G. Bilalbegovic, A. Maksimovic, and L. A. Valencic, Tetrahedral hydrocarbon nanoparticles in space: X-ray spectra, Mon. Not. R. Astron. Soc. **476**, 5358 (2018).

[57] C. W. Bauschlicher, Jr., Y. Liu, A. Ricca, A. L. Mattioda, and L. J. Allamandola, Electronic and vibrational spectroscopy of diamondoids and the interstellar infrared bands between 3.35 and 3.55 μm, Astrophys. J. **671**, 458 (2007).

[58] M. Heidari Saani, T. Ghodselahi, and K. Esfarjani, Strain-induced instability of spherical nanodiamond hydrocarbons: Effect of surface CH_n and charging, Phys. Rev. B **79**, 125429 (2009).

[59] J. Wang, L. Ma, and J. Zhao, First-principles study of nanodiamond doped with B and N, Int. J. Mod. Phys. B **24**, 6099 (2010).

[60] P.-Y. Chen, L. Zhang, S.-G. Zhu, and G.-B. Cheng, Intermolecular interactions, thermodynamic properties, crystal structure, and detonation performance of Cl-20/TEX cocrystal explosive, Can. J. Chem. **93**, 632 (2015).

[61] P. Giannozzi *et al.*, Quantum Espresso: A modular and open-source software project for quantum simulations of materials, J. Phys.: Condens. Matter **21**, 395502 (2009).

[62] J. P. Perdew and A. Zunger, Self-interaction correction to density-functional approximations for many-electron systems, Phys. Rev. B **23**, 5048 (1981).

[63] A. Dal Corso, S. Baroni, R. Resta, and S. de Gironcoli, *Ab initio* calculation of phonon dispersions in II-VI semiconductors, Phys. Rev. B **47**, 3588 (1993).

[64] J. P. Perdew, K. Burke, and M. Ernzerhof, Generalized Gradient Approximation Made Simple, Phys. Rev. Lett. **77**, 3865 (1996).

[65] C. Hartwigsen, S. Goedecker, and J. Hutter, Relativistic separable dual-space Gaussian pseudopotentials from H to Rn, Phys. Rev. B **58**, 3641 (1998).

[66] A. D. Becke, Density-functional thermochemistry. III. The role of exact exchange, J. Chem. Phys. **98**, 5648 (1993).

[67] C. Lee, W. Yang, and R. G. Parr, Development of the Colle-Salvetti correlation-energy formula into a functional of the electron density, Phys. Rev. B **37**, 785 (1988).

[68] P. B. Allen, Solids with thermal or static disorder. I. One-electron properties, Phys. Rev. B **18**, 5217 (1978).

[69] P. B. Allen and M. Cardona, Temperature dependence of the direct gap of Si and Ge, Phys. Rev. B **27**, 4760 (1983).

[70] M. Cardona and M. L. W. Thewalt, Isotope effects on the optical spectra of semiconductors, Rev. Mod. Phys. **77**, 1173 (2005).

[71] Z. Wang, M. Rafipoor, P. Garcia-Risueño, J.-P. Merkl, P. Han, H. Lange, and G. Bester, Phonon-assisted auger process enables ultrafast charge transfer in CdSe quantum dot/organic molecule, J. Phys. Chem. C **123**, 17127 (2019).

[72] C. Faber, J. Laflamme Janssen, M. Côté, E. Runge, and X. Blase, Electron-phonon coupling in the C_{60} fullerene within the many-body *GW* approach, Phys. Rev. B **84**, 155104 (2011).

[73] S. Logothetidis, J. Petalas, H. M. Polatoglou, and D. Fuchs, Origin and temperature dependence of the first direct gap of diamond, Phys. Rev. B **46**, 4483 (1992).

[74] M. Cardona, Electron-phonon interaction in tetrahedral semiconductors, Solid State Commun. **133**, 3 (2005).

[75] M. Cardona, Renormalization of the optical response of semiconductors by electron-phonon interaction, Phys. Status Solidi A **188**, 1209 (2001).

[76] S. Banerjee, T. Stüker, and P. Saalfrank, Vibrationally resolved optical spectra of modified diamondoids obtained from time-dependent correlation function methods, Phys. Chem. Chem. Phys. **17**, 19656 (2015).

[77] S. Zollner, M. Cardona, and S. Gopalan, Isotope and temperature shifts of direct and indirect band gaps in diamond-type semiconductors, Phys. Rev. B **45**, 3376 (1992).